



Distributed optimal control allocation for 6-dof spacecraft with redundant thrusters

Xiaoyu Lang, Anton de Ruiter*

Ryerson University, Toronto, Ontario, M5B 2K3, Canada

ARTICLE INFO

Article history:

Received 23 July 2020

Received in revised form 26 November 2020

Accepted 11 July 2021

Available online 21 July 2021

Communicated by Raghvendra Cowlagi

Keywords:

Control allocation

6-dof spacecraft control

Distributed algorithm

ABSTRACT

Control allocation for 6-dof spacecraft maneuvers is considered. Retired spacecraft, whose own control system is inoperable, can be reused by installing multiple cellular thruster modules to provide thrusts for translational and rotational control. Such cellular thruster modules collaborate with their neighbors in a network topology to calculate an optimal distribution matrix for thrust allocation. A pseudo-inverse optimal thrust allocation scheme is extended to a distributed iteration algorithm to enable this optimal problem to be solved by cellular thruster modules in a distributed manner. Subsequently, a norm-based distributed pseudo-inverse optimal thrust allocation scheme is developed to solve the same optimal thrust allocation problem. The syntheses of two distributed optimal thrust allocation schemes are discussed. Numerical simulations are demonstrated in the end to show the effectiveness of two proposed distributed thrust allocation schemes. Performance comparisons between two schemes are analyzed as well.

© 2021 Elsevier Masson SAS. All rights reserved.

1. Introduction

Maintenance of retired spacecraft has attracted more research on on-orbit servicing technology. Such retired spacecraft usually have some still functional components and are valuable to be reused. To proceed the maintenance process, the primary stage is that using servicing space robots to approximate and capture the retired spacecraft [1]. This stage has high requirements for the control performance of servicing space robots. It not only needs dedicated design of mechanisms [2], but also requires a powerful control system in space robots, particularly when the retired spacecraft has already been tumbling [3]. To facilitate it, the concept of cellular space modules has been put forward for the reuse of retired spacecraft in some space missions, such as “Phoenix project” [4]. This project planned to employ multiple cellularized space modules (or called “Satlet”) aggregated to a single retired spacecraft to fulfill the functions which were completed by subsystems in conventional monolithic spacecraft [4]. This cellularization idea was inspired by biological cells and intended to degenerate the conventional monolithic spacecraft to decentralized small modules. These modules can communicate and interact with each other through wireless links and aggregate a distributed network system to reuse the retired spacecraft. The iBOSS (Intelligent Building Blocks for On-Orbit Satellite Servicing) project proposed “plug-and-play” interfaces for the transmission of power, data and thermal among cellular space modules [5].

Rendezvous and proximity operations play dominant roles in some on-orbit servicing missions, where the translation and rotation of spacecraft as well as their mutual coupling effects should be considered concurrently. In traditional space research, spacecraft translation and rotation were studied separately and their couplings were usually omitted in dynamic modeling and controller design, which would bring about poor precision and efficiency issues in control performance [6]. To accommodate such issues, the coupled 6-dof relative motion dynamics are important to be analyzed to establish powerful control scheme for the stability of spacecraft [7–12]. The 6-dof dynamic model can be simplified as the combination of classical Euler’s equations and relative motion equations (like Hill’s equations) to design control algorithm in complicated fashions [13–15]. As the extension of traditional quaternions, dual quaternions had been widely used to describe 6-dof spacecraft motion. The dual-quaternion-based sliding mode control for an integrated 6-dof spacecraft motion was discussed in [16]. Using the dual-quaternion formulation, various kinds of control algorithms have been exploited, such as adaptive control

* Corresponding author.

E-mail addresses: xiaoyu.lang@ryerson.ca (X. Lang), aderuiter@ryerson.ca (A. de Ruiter).

with inertia identification [17], and finite-time output feedback control [18]. The way to design dual-quaternion-based controller could always be inspired by quaternion-based controllers because of the similar mathematical properties. The unwinding problem of quaternions, however, is also inherited by the dual quaternions [19]. The special Euclidean group, or SE(3), is an alternative to dual quaternions to model the 6-dof dynamics [20]. An observer-based robust adaptive control scheme was proposed in [21] using SE(3) formulation with the consideration of actuator saturation and misalignment.

Thrusters are quite common actuators for spacecraft steering. Compared with other types of actuator, such as reaction wheels, all-thruster actuation systems are simple to be implemented in 6-dof motion control [22,23]. In particular, when thrust vectors produced by propulsion systems do not cross through the mass center of spacecraft, torques can be generated together with thrusts and their corresponding moment arms [24]. This causes the dynamic coupling between translation and rotation of spacecraft [13]. It is obvious that at least six thrusters are needed to accomplish 6-dof spacecraft rendezvous and proximity operations. However, thruster redundancy is a quite common practice for spacecraft maneuvering, particularly for large-mass monolithic spacecraft. Using a redundant thruster configuration needs a control allocation algorithm to apportion the desired forces and torques into multiple thrusters to produce desired control commands. The control allocation problem has been investigated substantially in [25]. There are fruitful results about control allocation, such as pseudo-inverse allocation [26], dynamic control allocation [27–29], programming control allocation [30,31], etc. For a 6-dof spacecraft with thruster-only actuation, a Lyapunov-based method was proposed in [13] for thrust allocation and thruster selection. An optimal combination table was proposed in [8] to choose specific thrusters and calculate the firing time intervals based on linear programming. A simplex method has been implemented to have an optimal thruster management function [32]. A pre-computing distributed matrix for thruster control allocation was formulated in [33,34] using min-max optimization. This method is a fusion of the selection matrix method [8] and the process of Linear Programming [35], which only needs to calculate a single constant distribution matrix. Based on the concept of cellularized space robots, Chang et al. [36] proposed a control allocation algorithm for the cellular space modules which contain corresponding actuators to produce torques for 3-dof attitude takeover control in a distributed manner. The scheme proposed in [36] was actually inspired by the idea on the estimation of the truth values over sensor networks [37], which has been exploited extensively in distributed computing of multi-agent systems. This kind of multi-agent-based algorithm can also be used to solve the distributed optimization problems for resource allocation in a decentralized manner [38]. Fault-tolerant attitude tracking control problem for over-actuated spacecraft was addressed in Ref. [39] when the actuator failure happens, and the problem was tackled with an on-line control allocation scheme and a novel fault-tolerant control algorithm. A robust control allocation was proposed in Ref. [40] to deal with spacecraft attitude tracking control when an actuator has fault but fault detection and diagnosis scheme is imprecise. An application of direct force control was presented with a novel closed-loop control allocation method for force and moment increment distribution [41]. A control allocation scheme with a fuzzy controller was presented in Ref. [42] to solve the attitude control problem in a Cubesat-based space debris removal mission which is an over-actuated space system. A quadratic-programming-based control allocation was used by Ref. [43] to generate control commands for thrusters from the control signals calculated by a novel dynamic-programming-based optimal method. In Ref. [44], the authors proposed a dynamic near-optimal control allocator augmented with penalty terms for spacecraft control. However, all of the above 6-dof control allocation algorithms are centralized approaches. When the spacecraft is equipped with multiple redundant cellular space modules for motion control, a scheme is needed for control allocation in a distributed pattern. The distributed control allocation scheme for spacecraft 6-dof translation and rotation control using cellular thruster modules is still not available. The dynamic coupling of forces and torques induced by thruster-only actuation configuration poses a challenge to obtain the optimal thrust allocation matrix in a distributed way. To tackle this challenge, this paper develops the distributed optimal thrust allocation algorithm for 6-dof spacecraft maneuvers with multiple cellular thruster modules which consist of thrusters and communication subsystems. Each cellular thruster module could interact with its neighbors within a certain network topology to yield an optimal thrust allocation matrix using the proposed distributed algorithm.

The rest of this work is structured as follows. Some preliminaries about spacecraft 6-dof dynamics using SE(3) are reviewed in Section 2. Section 3 is the main result of this paper. In Section 3.2, a pseudo-inverse optimal thrust allocation is implemented in a distributed way which enables all cellular thruster modules to calculate an optimal thrust allocation matrix jointly. Based on this scheme, a norm-based distributed pseudo-inverse optimal thrust allocation scheme is developed in Section 3.3. In Section 4, numerical simulations are conducted to show the effectiveness of the two proposed distributed thrust allocation algorithms. Moreover, comparisons between the two schemes are also carried out to manifest the advantages of the norm-based scheme. Conclusions are given in Section 5.

2. Preliminaries

2.1. Dynamics and kinematics for rigid-body spacecraft on SE(3)

Consider a rigid-body spacecraft's 6-dof motion which is depicted in Fig. 1 in the three-dimensional space. To describe this motion, two coordinate frames are introduced at first. The frame $\mathcal{F}_I (X_I, Y_I, Z_I)$ denotes the Earth-centered inertial frame whose origin is at the center of mass of Earth. The frame $\mathcal{F}_B (X_B, Y_B, Z_B)$ is the body-fixed frame and its origin sits at the mass center of the rigid-body spacecraft. The translation of spacecraft is denoted by $\boldsymbol{\rho} \in \mathbb{R}^3$ in \mathcal{F}_I . The rotation of spacecraft is described by the rotation matrix $\mathbf{C} \in \text{SO}(3)$ from \mathcal{F}_B to \mathcal{F}_I where the special orthogonal group SO(3) is given by $\text{SO}(3) = \{\mathbf{C} \in \mathbb{R}^{3 \times 3} | \mathbf{C}^T \mathbf{C} = \mathbf{I}, \det(\mathbf{C}) = 1\}$ (\mathbf{I} is the identity matrix). SO(3) is a special matrix Lie group and its corresponding vector space (also referred to as associated Lie algebra) is denoted by $\mathfrak{so}(3)$. For a general vector $\mathbf{a} = [a_1, a_2, a_3]^T$, its skew symmetric matrix \mathbf{a}^\times is defined as

$$\mathbf{a}^\times = \begin{bmatrix} 0 & -a_3 & a_2 \\ a_3 & 0 & -a_1 \\ -a_2 & a_1 & 0 \end{bmatrix} \quad (1)$$

$\mathfrak{so}(3)$ is the vector space of skew symmetric matrices, which is given by $\mathfrak{so}(3) = \{\tilde{\mathbf{a}} = \mathbf{a}^\times \in \mathbb{R}^{3 \times 3} | \mathbf{a} \in \mathbb{R}^3, \tilde{\mathbf{a}}^T = -\tilde{\mathbf{a}}\}$. The operator $(\cdot)^\times$ can be regarded as $\mathbb{R}^3 \rightarrow \mathfrak{so}(3)$.

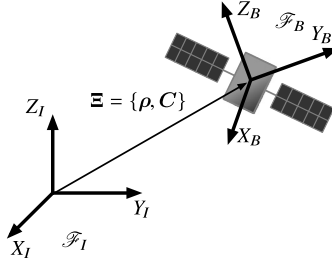


Fig. 1. Rigid-body spacecraft 6-dof motion.

The rotation matrix $\mathbf{C} \in \text{SO}(3)$ can be represented by Euler axis/angle (\mathbf{e}, θ) as $\mathbf{C} = \cos \theta \mathbf{1} + (1 - \cos \theta) \mathbf{e} \mathbf{e}^T + \sin \theta \mathbf{e}^\times$. Let $\boldsymbol{\phi} = \theta \mathbf{e}$ and $\boldsymbol{\phi}$ can be represented by the rotation matrix \mathbf{C} as

$$\boldsymbol{\phi}^\times = \begin{cases} 0 & \theta = 0 \\ \frac{\theta}{2 \sin \theta} (\mathbf{C} - \mathbf{C}^T) & \theta \in (-\pi, \pi), \theta \neq 0 \end{cases} \quad (2)$$

where $\theta = \arccos(0.5(\text{trace}(\mathbf{C}) - 1)) = \|\boldsymbol{\phi}\|$ ($\|\cdot\|$ is the Euclidean norm).

The translation and rotation of the spacecraft can be described in a compact form as

$$\Xi = \begin{bmatrix} \mathbf{C} & \boldsymbol{\rho} \\ \mathbf{0}_{1 \times 3} & 1 \end{bmatrix} \in \text{SE}(3) \quad (3)$$

whose alternative notation is $\Xi = \{\boldsymbol{\rho}, \mathbf{C}\}$, as used in Fig. 1. Here, $\text{SE}(3)$ is another special matrix Lie group: the special Euclidean group, which is defined as

$$\text{SE}(3) = \{\Xi \in \mathbb{R}^{4 \times 4} | \mathbf{C} \in \text{SO}(3), \boldsymbol{\rho} \in \mathbb{R}^3\}$$

The fundamental knowledge of $\text{SE}(3)$ can be referred to Ref. [45] for more details, and the definitions and formulas related to this work are reviewed as follows. Define $\boldsymbol{\eta} = [\boldsymbol{\phi}^T, \boldsymbol{\varphi}^T]^T \in \mathbb{R}^6$. The associated Lie algebra of $\Xi \in \text{SE}(3)$ is expressed as $\mathfrak{se}(3) = \{\boldsymbol{\eta}^\wedge \in \mathbb{R}^{4 \times 4} | \boldsymbol{\eta} \in \mathbb{R}^6\}$. The notation $\boldsymbol{\eta}^\wedge$ is given by

$$\boldsymbol{\eta}^\wedge = \begin{bmatrix} \boldsymbol{\phi} \\ \boldsymbol{\varphi} \end{bmatrix}^\wedge = \begin{bmatrix} \boldsymbol{\phi}^\times & \boldsymbol{\varphi} \\ \mathbf{0}_{1 \times 3} & 0 \end{bmatrix} \in \mathfrak{se}(3) \quad (4)$$

where $\boldsymbol{\varphi}$ is the vector describing the translation, which is given by [21]

$$\boldsymbol{\varphi} = \mathcal{J}^{-1} \boldsymbol{\rho}, \quad \mathcal{J} = \mathbf{1} + \frac{1 - \cos \theta}{\theta^2} \boldsymbol{\phi}^\times + \frac{\theta - \sin \theta}{\theta^3} \boldsymbol{\phi}^\times \boldsymbol{\phi}^\times \quad (5)$$

The elements of $\Xi \in \text{SE}(3)$ can be related to the elements of $\boldsymbol{\eta}^\wedge \in \mathfrak{se}(3)$ ($\boldsymbol{\eta} \in \mathbb{R}^6$) via an exponential map:

$$\Xi = \exp(\boldsymbol{\eta}^\wedge) \quad (6)$$

Let $(\cdot)^\wedge$ undo $(\cdot)^\vee$ such that $(\boldsymbol{\eta}^\wedge)^\vee = \boldsymbol{\eta}$. The exponential map in Eq. (6) in an inverse direction is given by

$$\boldsymbol{\eta} = \ln(\Xi)^\vee \quad (7)$$

Let \mathbf{v} denote velocity and $\boldsymbol{\omega}$ denote angular velocity of the spacecraft, and both are expressed in the body frame \mathcal{F}_B . The kinematics are described as

$$\dot{\boldsymbol{\rho}} = \mathbf{C} \mathbf{v}, \quad \dot{\mathbf{C}} = \mathbf{C} \boldsymbol{\omega}^\times \quad (8)$$

Let $\boldsymbol{\xi} = [\boldsymbol{\omega}^T, \mathbf{v}^T]^T \in \mathbb{R}^6$. The notion $\boldsymbol{\xi}^\wedge$ is defined as

$$\boldsymbol{\xi}^\wedge = \begin{bmatrix} \boldsymbol{\omega} \\ \mathbf{v} \end{bmatrix}^\wedge = \begin{bmatrix} \boldsymbol{\omega}^\times & \mathbf{v} \\ \mathbf{0}_{1 \times 3} & 0 \end{bmatrix} \in \mathfrak{se}(3)$$

The kinematic equation shown in Eq. (8) can be rewritten via the exponential map as [46]:

$$\dot{\boldsymbol{\eta}} = \mathbf{G}(\boldsymbol{\eta}) \boldsymbol{\xi} \quad (9)$$

where

$$\mathbf{G}(\boldsymbol{\eta}) = \begin{bmatrix} \mathbf{P}(\boldsymbol{\phi}, \theta) & \mathbf{0} \\ \mathbf{Q}(\boldsymbol{\phi}, \boldsymbol{\varphi}, \theta) & \mathbf{P}(\boldsymbol{\phi}, \theta) \end{bmatrix} \quad (10a)$$

$$\mathbf{P}(\boldsymbol{\phi}, \theta) = \mathbf{1} + \frac{1}{2} \boldsymbol{\phi}^\times + \left(\frac{1}{\theta^2} - \frac{1 + \cos \theta}{2\theta \sin \theta} \right) \boldsymbol{\phi}^\times \boldsymbol{\phi}^\times \quad (10b)$$

$$\begin{aligned} \mathbf{Q}(\boldsymbol{\phi}, \boldsymbol{\varphi}, \theta) = & \frac{1}{2}(\mathcal{J}\boldsymbol{\varphi})^\times \mathbf{P}(\boldsymbol{\phi}, \theta) + \left(\frac{1}{\theta^2} - \frac{1 + \cos \theta}{2\theta \sin \theta} \right) (\boldsymbol{\phi}\boldsymbol{\varphi}^\top + \boldsymbol{\phi}^\top \boldsymbol{\varphi} \mathbf{P}(\boldsymbol{\phi}, \theta)) - \frac{(1 + \cos \theta)(\theta - \sin \theta)}{2\theta \sin^2 \theta} \mathcal{J}\boldsymbol{\varphi}\boldsymbol{\phi}^\top + \\ & \left(\frac{(1 + \cos \theta)(\theta + \sin \theta)}{2\theta^3 \sin^2 \theta} - \frac{2}{\theta^4} \right) \boldsymbol{\phi}^\top \boldsymbol{\varphi} \boldsymbol{\phi} \boldsymbol{\phi}^\top \end{aligned} \quad (10c)$$

The dynamics of the rigid-body spacecraft are governed by [21]:

$$\begin{aligned} \mathbf{I}\dot{\boldsymbol{\omega}} + \boldsymbol{\omega}^\times \mathbf{I}\boldsymbol{\omega} &= \mathbf{t}_c + \mathbf{t}_g + \mathbf{t}_d \\ m\dot{\mathbf{v}} + m\boldsymbol{\omega}^\times \mathbf{v} &= \mathbf{f}_c + \mathbf{f}_g + \mathbf{f}_d \end{aligned} \quad (11)$$

where $\mathbf{I} \in \mathbb{R}^{3 \times 3}$ is the moment of inertia matrix of the spacecraft, m is the mass of the spacecraft, $\mathbf{f}_c \in \mathbb{R}^3$ and $\mathbf{t}_c \in \mathbb{R}^3$ are the control force and torque respectively. The control force \mathbf{f}_c and torque \mathbf{t}_c are obtained from a feedback control law as the high-level control signals preparing for thrust allocation. It is assumed that the rigid-body spacecraft operates in the vicinity of the Earth. The gravitational force \mathbf{f}_g and gravity-gradient torque \mathbf{t}_g are worth to be considered. The specific form of \mathbf{f}_g is expressed as follows [47].

$$\mathbf{f}_g = \mathbf{f}_G + \mathbf{f}_{J_2} \quad (12)$$

where

$$\mathbf{f}_G = -\frac{m\mu}{\|\boldsymbol{\rho}\|^3} \boldsymbol{\rho}_b - 3\frac{\mu}{\|\boldsymbol{\rho}\|^5} \left(\frac{1}{2} \text{trace}(\mathbf{I}) \mathbf{1} + \mathbf{I} \right) \boldsymbol{\rho}_b + \frac{15}{2} \frac{\mu \boldsymbol{\rho}_b^\top \mathbf{I} \boldsymbol{\rho}_b}{\|\boldsymbol{\rho}\|^7} \boldsymbol{\rho}_b \quad (13)$$

and

$$\mathbf{f}_{J_2} = m\mathbf{C}^\top \begin{bmatrix} -\frac{3\mu J_2 R_E^2 \rho_x}{2\|\boldsymbol{\rho}\|^5} \left(1 - \frac{5\rho_z^2}{\|\boldsymbol{\rho}\|^2} \right) \\ -\frac{3\mu J_2 R_E^2 \rho_y}{2\|\boldsymbol{\rho}\|^5} \left(1 - \frac{5\rho_z^2}{\|\boldsymbol{\rho}\|^2} \right) \\ -\frac{3\mu J_2 R_E^2 \rho_z}{2\|\boldsymbol{\rho}\|^5} \left(3 - \frac{5\rho_z^2}{\|\boldsymbol{\rho}\|^2} \right) \end{bmatrix} \quad (14)$$

The standard gravitational parameter of the Earth is herein denoted by $\mu = 3.986 \times 10^{14} \text{ m}^3 \text{ s}^{-2}$. $J_2 = 1.08263 \times 10^{-3}$ is the J_2 perturbation constant due to the oblateness of the Earth. $R_E = 6378.14 \text{ km}$ is the Earth's equatorial radius. $\boldsymbol{\rho}_b = \mathbf{C}^\top \boldsymbol{\rho}$, and ρ_x, ρ_y and ρ_z are the entries of the position vector $\boldsymbol{\rho}$. The gravity gradient torque \mathbf{t}_g is expressed as [24]:

$$\mathbf{t}_g = 3\frac{\mu}{\|\boldsymbol{\rho}\|^5} \boldsymbol{\rho}_b^\times \mathbf{I} \boldsymbol{\rho}_b \quad (15)$$

The external disturbance torques and forces are indicated by \mathbf{t}_d and \mathbf{f}_d respectively.

Transform Eq. (11) into a compact form with $\boldsymbol{\xi}$ [21]:

$$\mathbf{M}^* \dot{\boldsymbol{\xi}} = \text{ad}_{\boldsymbol{\xi}}^* \mathbf{M}^* \boldsymbol{\xi} + \boldsymbol{\Gamma}_g + \boldsymbol{\Gamma}_c + \boldsymbol{\Gamma}_d \quad (16)$$

where

$$\mathbf{M}^* = \begin{bmatrix} \mathbf{I} & \mathbf{0} \\ \mathbf{0} & m\mathbf{1} \end{bmatrix} \in \mathbb{R}^{6 \times 6}, \quad \boldsymbol{\Gamma}_g = \begin{bmatrix} \mathbf{t}_g \\ \mathbf{f}_g \end{bmatrix}, \quad \boldsymbol{\Gamma}_c = \begin{bmatrix} \mathbf{t}_c \\ \mathbf{f}_c \end{bmatrix}, \quad \boldsymbol{\Gamma}_d = \begin{bmatrix} \mathbf{t}_d \\ \mathbf{f}_d \end{bmatrix}$$

The term $\text{ad}_{\boldsymbol{\xi}}^*$ is defined as

$$\text{ad}_{\boldsymbol{\xi}}^* = -\text{ad}_{\boldsymbol{\xi}}^\top, \quad \text{ad}_{\boldsymbol{\xi}} = \boldsymbol{\xi}^\wedge = \begin{bmatrix} \boldsymbol{\omega}^\times & \mathbf{0} \\ \mathbf{v}^\times & \boldsymbol{\omega}^\times \end{bmatrix} \in \mathbb{R}^{6 \times 6} \quad (17)$$

Let $(\cdot)^\vee$ undo $(\cdot)^\wedge$ operation such that $\boldsymbol{\xi} = (\boldsymbol{\xi}^\wedge)^\vee$.

2.2. Problem statement

This paper is concerned with a retired spacecraft which is assumed to be unable to maintain its own position or attitude. The retired spacecraft would be reused by installing multiple cellular thruster modules. The spacecraft's 6-dof motion (i.e. 3-dof translation and 3-dof rotation) control are taken over and then operated by these multiple cellular thruster modules. Each cellular thruster module not only contains a thruster which can generate a single-direction thrust, but also can communicate and interact with its neighbor in a topology. The dynamic model described by Eq. (16) governs the 6 degree-of-freedom motion such that $\boldsymbol{\Gamma}_c \in \mathbb{R}^6$. It is not an uncommon practice for spacecraft with actuation redundancy, which means that the number of actuators is greater than the degree of freedom of $\boldsymbol{\Gamma}_c$. Similarly, the number of the cellular thruster modules is over 6, denoted by $n(n > 6)$ in this paper, to produce desired control commands. There is an n -dimensional thrust vector $\boldsymbol{\tau} = [\tau_1, \tau_2, \dots, \tau_n]^\top$ where $\tau_\alpha (\alpha = 1, 2, \dots, n)$ represents the thrust produced by the α -th cellular thruster module. A thruster configuration matrix $\mathbf{H} \in \mathbb{R}^{6 \times n}$ is formed by the specific placement of the cellular thruster modules relative to the spacecraft mass center as

$$\mathbf{H} = \begin{bmatrix} \mathbf{H}_\tau \\ \mathbf{H}_f \end{bmatrix} \quad (18)$$

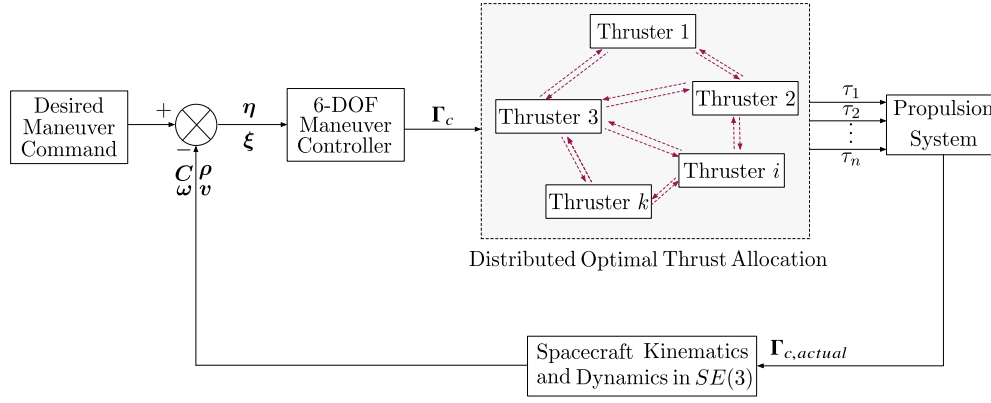


Fig. 2. The block diagram of the closed loop system.

where \mathbf{H}_τ and \mathbf{H}_f indicate the cellular thruster modules' locations and directions respectively. The actual force and torque $\mathbf{\Gamma}_{c,actual} \in \mathbb{R}^6$ can be given by

$$\mathbf{\Gamma}_{c,actual} = \mathbf{H}\boldsymbol{\tau} \quad (19)$$

Note that matrix \mathbf{H} is a constant parameter when the placements of cellular thruster modules are determined. Additionally, the matrix \mathbf{H} is assumed to be full rank. This assumption guarantees that the cellular thruster modules are able to provide 6-dof thrusts for spacecraft maneuvering.

To tackle the 6-dof spacecraft control allocation problem, a hierarchical takeover control scheme is needed and should be divided into two distinctive parts: the control law and thrust allocation. The control law produces the required forces and torques $\mathbf{\Gamma}_c \in \mathbb{R}^6$ (or called high-level control signals) for spacecraft maneuver. A simple and commonly used thrust allocation is a logic to calculate a distribution matrix $\mathbf{D}_m \in \mathbb{R}^{n \times 6}$ such that

$$\boldsymbol{\tau} = \mathbf{D}_m \mathbf{\Gamma}_c \quad (20)$$

Note that the matrix \mathbf{D}_m is the parameter which is to be designed in this paper. This thrust allocation process yields the thrust vector $\boldsymbol{\tau}$, which is named low-level control signals. The high-level control signals $\mathbf{\Gamma}_c$ in this hierarchical control scheme would be calculated at the first stage through a feedback control algorithm. The low-level control signals $\boldsymbol{\tau}$ would be obtained afterward via an interactive computation among all cellular thruster modules through wireless links within the topology. Consider a network topology having n cellular thruster modules which are mounted on the rigid-body spacecraft. This network topology is assumed to be an undirected graph \mathcal{G} with an edge set \mathcal{E} and a node set \mathcal{V} . The n cellular thruster modules are viewed as the nodes of \mathcal{G} as $\mathcal{V} = \{1, 2, \dots, n\}$. The connection of a pair two nodes $\{k, l\}$ composes an undirected edge. As the node of \mathcal{G} , each cellular thruster module can not only produce thrust along with a certain direction, but also communicate with its neighbors in \mathcal{G} . The graph \mathcal{G} is assumed to be connected. All above fundamental knowledge of graph theory is based on [48].

Each cellular thruster module can communicate and interact with its connected neighbor. In this process, a distributed thrust allocation algorithm will be developed to calculate the distribution matrix \mathbf{D}_m , which is the major part of this paper. The closed-loop system outlining this paper is diagrammed in Fig. 2.

The matrix \mathbf{H} is not a square matrix when spacecraft is equipped with redundant cellular thruster modules. The simplest approach to generate \mathbf{D}_m is pseudo inverse such that $\mathbf{D}_m = \mathbf{H}^\dagger$. However, such \mathbf{D}_m is not obtained from an optimization process in which the constraint for thrusters is considered. Considering the scenario that the spacecraft 6-dof maneuvers are fulfilled by multiple cellular thruster modules, this paper will study two distributed optimal thrust allocation schemes (dashed line square in Fig. 2), which are the major contribution and are described in the subsequent section. The term "distributed" means that the proposed schemes are executed locally by each cellular thruster module in a network to solve the optimal thrust allocation problem. This network has no central fusion but consists of multiple cellular thruster modules which collaboratively compute optimal thrust allocation matrix and produce desired thrusts.

3. Distributed pseudo-inverse optimal thrust allocation logic

Two distributed optimal thrust allocation logics will be discussed in this section for 6-dof spacecraft maneuvers using multiple cellular thruster modules. The desired control torques and forces are reformed as a new vector preparing for the following thrust allocation scheme. The first proposed thrust allocation scheme is extending the pseudo-inverse optimal control allocation in [34] to a distributed algorithm which can be executed by the multiple cellular thruster modules in a distributed manner. The second one is developed as a new scheme: norm-based distributed pseudo-inverse optimal thrust allocation scheme. The entire thrust allocation procedures are synthesized for 6-dof spacecraft maneuvers as well.

3.1. Precondition for thrust allocation

Motivated by [33][34], the elements of $\mathbf{\Gamma}_c$ (required forces and torques) are categorized by signs to form a new vector for the distributed optimal thrust allocation scheme. The required forces and torques $\mathbf{\Gamma}_c = [\mathbf{t}_c^T, \mathbf{f}_c^T]^T \in \mathbb{R}^{6 \times 1}$, which are obtained from a feedback control law (high-level control signals), can be refined as [33]:

$$\tilde{\mathbf{r}}_c = \begin{bmatrix} \mathbf{t}_c/l \\ \mathbf{f}_c \end{bmatrix} \quad (21)$$

where the scaling factor l (a constant number) can avoid the possible singularity or allocation error which may be caused by the different magnitudes of force and torque. It can be further specified as $\tilde{\mathbf{r}}_c = [\tilde{r}_{c1}, \tilde{r}_{c2}, \tilde{r}_{c3}, \tilde{r}_{c4}, \tilde{r}_{c5}, \tilde{r}_{c6}]^T$. Let

$$\tilde{\mathbf{r}}_{ci}^{\oplus} = \begin{cases} \tilde{r}_{ci} & \tilde{r}_{ci} \geq 0 \\ 0 & \tilde{r}_{ci} < 0 \end{cases} \quad (i = 1, 2, \dots, 6) \quad (22a)$$

$$\tilde{\mathbf{r}}_{ci}^{\ominus} = \begin{cases} 0 & \tilde{r}_{ci} \geq 0 \\ \tilde{r}_{ci} & \tilde{r}_{ci} < 0 \end{cases} \quad (i = 1, 2, \dots, 6) \quad (22b)$$

Define a new vector $\tilde{\mathbf{r}}_c^{\oplus} \in \mathbb{R}^{12 \times 1}$ whose elements are all non-negative as [33]:

$$\tilde{\mathbf{r}}_c^{\oplus} = [\tilde{r}_{c1}^{\oplus}, \tilde{r}_{c2}^{\oplus}, \tilde{r}_{c3}^{\oplus}, \tilde{r}_{c4}^{\oplus}, \tilde{r}_{c5}^{\oplus}, \tilde{r}_{c6}^{\oplus}, |\tilde{r}_{c1}^{\ominus}|, |\tilde{r}_{c2}^{\ominus}|, |\tilde{r}_{c3}^{\ominus}|, |\tilde{r}_{c4}^{\ominus}|, |\tilde{r}_{c5}^{\ominus}|, |\tilde{r}_{c6}^{\ominus}|]^T \quad (23)$$

As shown in Eq. (22), all the elements of $\tilde{\mathbf{r}}_c$ are classified into a positive value group \tilde{r}_{ci}^{\oplus} ($i = 1, \dots, 6$) and a non-positive value group \tilde{r}_{ci}^{\ominus} ($i = 1, \dots, 6$). The first six elements of the new non-negative vector $\tilde{\mathbf{r}}_c^{\oplus}$ constitute the positive value group \tilde{r}_{ci}^{\oplus} and the last six elements of $\tilde{\mathbf{r}}_c^{\oplus}$ are the absolute values of the non-positive value group \tilde{r}_{ci}^{\ominus} . Since the single non-gimbaled thruster can only provide non-negative force, the definition of the vector $\tilde{\mathbf{r}}_c^{\oplus}$ as shown in Eq. (23) is prepared for obtaining non-negative thrusts $\boldsymbol{\tau}$ when $\tilde{\mathbf{r}}_c^{\oplus}$ is multiplied with a distribution matrix \mathbf{D} whose elements are all non-negative.

For the vector $\boldsymbol{\tau} = [\tau_1, \tau_2, \dots, \tau_n]^T$, there is a new optimal distribution matrix $\mathbf{D} = [D_1, \dots, D_{12}] \in \mathbb{R}^{n \times 12}$ such that [33]

$$\boldsymbol{\tau} = \mathbf{D} \tilde{\mathbf{r}}_c^{\oplus} \quad (24)$$

Since a general thruster can only produce thrust along a single direction, the value of thrust provided by each cellular thruster module must be greater than or equal to zero, i.e. $\tau_{\alpha} \geq 0 (\alpha = 1, 2, \dots, n)$. This constraint confines that all the entries of \mathbf{D} should be non-negative [33].

Recall the configuration matrix $\mathbf{H} \in \mathbb{R}^{6 \times n}$ for all cellular thruster modules. Take singular value decomposition of \mathbf{H} as [33]:

$$\mathbf{H} = \mathbf{U} \boldsymbol{\Sigma} \mathbf{V}^T = \mathbf{U} [\boldsymbol{\Sigma}, \mathbf{0}_{6 \times (n-6)}] \begin{bmatrix} \mathbf{V}_0 \\ \mathbf{V}_{\theta} \end{bmatrix} \quad (25)$$

where $\boldsymbol{\Sigma} \in \mathbb{R}^{6 \times 6}$ is a positive-definite diagonal matrix, matrix $\mathbf{V}_0 \in \mathbb{R}^{n \times 6}$ satisfies $\mathbf{V}_0^T \mathbf{V}_0 = \mathbf{I}$ (\mathbf{I} is an identity matrix), and the columns of $\mathbf{V}_{\theta} \in \mathbb{R}^{n \times (n-6)}$ span the null space of \mathbf{H} . The pseudo inverse of \mathbf{H} can be obtained as

$$\mathbf{H}^{\dagger} = \mathbf{V}_0 \boldsymbol{\Sigma}^{-1} \mathbf{U}^T \quad (26)$$

Having Eq. (19) in mind, the elements of $\boldsymbol{\tau}$ can be temporarily considered as the unknown variables of an undetermined linear equation. Due to redundancy configuration, the dimension of $\boldsymbol{\tau}$ is greater than the number of scalar equations in Eq. (19). The complete form of solution for Eq. (19) includes a particular part and a general one, which are given as follows [33].

$$\boldsymbol{\tau} = \mathbf{H}^{\dagger} \boldsymbol{\Gamma}_c + \mathbf{V}_{\theta} \mathbf{x} \quad (27)$$

where \mathbf{x} is an adjoint variable that can be tuned to make $\boldsymbol{\tau}$ confined by some special constraints.

3.2. Distributed pseudo-inverse optimal thrust allocation

Based on Eq. (24) and Eq. (27), a cost function $\Delta_{\beta} (\beta = 1, 2, \dots, 12)$ is established as [33]

$$\Delta_{\beta}(\mathbf{x}) = \mathbf{H}^{\dagger} \boldsymbol{\delta}_{\beta} + \mathbf{V}_{\theta} \mathbf{x} \quad (28)$$

where $\mathbf{x} \in \mathbb{R}^{(n-6) \times 1}$ is herein a decision variable, and $\boldsymbol{\delta}_{\beta}$ is the β -th column of a matrix $\boldsymbol{\delta} \in \mathbb{R}^{6 \times 12}$ which is given by:

$$\boldsymbol{\delta} = [\text{diag}\{1, 1, 1, 1, 1, 1\}, \text{diag}\{-1, -1, -1, -1, -1, -1\}] \quad (29)$$

The entries of $\boldsymbol{\delta}$ are compatible with the sign of vector $\tilde{\mathbf{r}}_c^{\oplus}$. The target of this paper is to obtain an optimal distribution matrix \mathbf{D} to minimize the thrusts provided by cellular thruster modules. Using the theory of min-max problem [34], the β -th column D_{β} of the distribution matrix \mathbf{D} can be formulated as

$$\begin{aligned} D_{\beta} &= \min_{\mathbf{x}} \max_m \Delta_{\beta}(\mathbf{x}) \\ \text{s.t. } \mathbf{V}_{\theta} \mathbf{x} &\geq -\mathbf{H}^{\dagger} \boldsymbol{\delta}_{\beta} \end{aligned} \quad (30)$$

where m represents the m -th element of the vector Δ_{β} . The constraint in Eq. (30) can restrict all the elements of D_{β} to be non-negative. The min-max optimization in Eq. (30) can find the worst case of Δ_{β} with an optimal vector \mathbf{x}^* such that each element of \mathbf{D} is minimized. Specifically, the *max* operation in Eq. (30) is to find the maximum element of the vector Δ_{β} . The *min* operation is to seek an optimal variable \mathbf{x}^* to have the minimum value of the maximum element. When the maximum element of Δ_{β} , which is the worst case of this

optimal problem, can be minimized by the optimal variable \mathbf{x}^* , the minimum values for all the elements of D_β can be guaranteed with this optimal variable \mathbf{x}^* . Hence, the minimum elements of $\boldsymbol{\tau}$ can be realized by calculating $\boldsymbol{\tau} = \mathbf{D}\tilde{\mathbf{I}}_c^\oplus$ [34].

As the core of the optimization problem, the cost function shown in Eq. (28) can be specified as

$$\Delta_\beta = [\Delta_\beta^{(1)}, \dots, \Delta_\beta^{(m)}, \dots, \Delta_\beta^{(n)}]^\top \in \mathbb{R}^{n \times 1} \quad (31)$$

where n is the total number of cellular thruster modules. Taking $\Delta_\beta^{(m)}$ as example, its subscript $(\cdot)_\beta$ corresponds to the column index of D_β and its superscript $(\cdot)^m$ indicates the m -th cellular thruster module. Given the setup of δ in Eq. (29), it is obvious that the only argument variable of $\Delta_\beta^{(m)}$ is the vector \mathbf{x} such that

$$\Delta_\beta^{(m)}(\mathbf{x}) = \left\{ \mathbf{H}^\top \delta_\beta + \mathbf{V}_\theta \mathbf{x} \right\}_m \quad (32)$$

where the subscript of $\{\cdot\}_m$ refers to the m -th element of this vector.

The topology connecting all cellular thruster modules is described by a graph \mathcal{G} , as introduced in Section 2.2. To be concise, the node $m \in \mathcal{V}$ will specifically refer to the cellular thruster module m ($m = 1, 2, \dots, n$). Note that “node” and “cellular thruster module” are used interchangeably afterward unless clarity has to be given. Let the node m hold a variable vector $\mathbf{x}^{(m)} \in \mathbb{R}^{(n-6) \times 1}$ which is regraded as the estimation of \mathbf{x}^* in the node m . Each node will iteratively update its own $\mathbf{x}^{(m)}$ via a distributed algorithm to reach a consensus on the common optimal vector \mathbf{x}^* . The optimization problem described in Eq. (30) can be recast in a distributed way:

$$\mathbf{x}_\beta^* = \arg \min_{\mathbf{x} \in \Upsilon_1} \max_{m \in \mathcal{V}} \Delta_\beta^{(m)}(\mathbf{x}), \quad D_\beta = \Delta_\beta(\mathbf{x}_\beta^*) \quad (33)$$

where the constraint set for \mathbf{x} is denoted by $\Upsilon_1 = \{\mathbf{x} | \mathbf{V}_\theta \mathbf{x} \geq -\mathbf{H}^\top \delta_\beta\}$. The node m holds its own cost function $\Delta_\beta^{(m)}(\mathbf{x})$. Introducing a new decision variable $\gamma_1 \in \mathbb{R}$ in the similar way as used in [49], the optimal solution of Eq. (33) is equivalent to

$$\begin{aligned} \min \quad & \gamma_1 \\ \text{s.t.} \quad & \Delta_\beta^{(m)}(\mathbf{x}) \leq \gamma_1, \forall \mathbf{x} \in \Upsilon_1, m \in \mathcal{V} \end{aligned} \quad (34)$$

The constraints in Eq. (34) can be compressed into the objective function to have another equivalent optimization problem [50]:

$$\min_{\mathbf{x} \in \Upsilon_1, \gamma_1 \in \mathbb{R}} \gamma_1 + \sum_{m=1}^n \kappa_m \Theta_\beta^{(m)}(\mathbf{x}, \gamma_1) \quad (35)$$

where $\Theta_\beta^{(m)}(\mathbf{x}, \gamma_1) = \max\{\Delta_\beta^{(m)}(\mathbf{x}) - \gamma_1, 0\}$ can be used to penalize the violation of the constraint $\Delta_\beta^{(m)}(\mathbf{x}) \leq \gamma_1$ set in Eq. (34). κ_m is the corresponding multiplier. According to [49], when $\kappa_m > 1$, the optimization problems shown in Eqs. (34) and (35) have the same optimal solution \mathbf{x}_β^* .

Let $\mathbf{x}^{(m)}(t) \in \mathbb{R}^{(n-6) \times 1}$ and $\gamma_1^{(m)}(t) \in \mathbb{R}^1$ denote the decision variables of cellular thruster module $m(m \in \mathcal{V})$ in the topology \mathcal{G} at the time t . When the distributed iteration scheme starts, all nodes (cellular thruster modules) in \mathcal{G} exchange their decision variables with their neighbors in the following way [50]:

$$\begin{aligned} \hat{\mathbf{x}}^{(m)}(t) &= \sum_{j \in \mathcal{N}_m} a_{mj} \mathbf{x}^{(m)}(t) \\ \hat{\gamma}_1^{(m)}(t) &= \sum_{j \in \mathcal{N}_m} a_{mj} \gamma_1^{(m)}(t) \end{aligned} \quad (36)$$

where $\hat{\mathbf{x}}^{(m)}(t)$ is the estimate of $\mathbf{x}^{(m)}(t)$ at time t , \mathcal{N}_m is the neighbor nodes of the node m , and a_{mj} is the entries of a doubly stochastic matrix \mathbf{A} which satisfies

$$\sum_{m=1}^n a_{mj} = 1, \quad \sum_{j=1}^n a_{mj} = 1 \quad (37)$$

Motivated by Ref. [50], a logical function $\mathcal{L}_1(\Delta_\beta^{(m)}, \gamma_1)$ can be defined as

$$\mathcal{L}_1(\Delta_\beta^{(m)}, \gamma_1) = \begin{cases} 1 & \Delta_\beta^{(m)} \geq \gamma_1 \\ 0 & \Delta_\beta^{(m)} < \gamma_1 \end{cases} \quad (38)$$

At the time $t + 1$, these decision variables $\hat{\mathbf{x}}^{(m)}$ are iterated as [50]

$$\hat{\mathbf{x}}^{(m)}(t + 1) = \mathcal{P}_{\Upsilon_1} \left[\hat{\mathbf{x}}^{(m)}(t) - \alpha(t) \kappa_m \frac{\partial \Delta_\beta^{(m)}(\mathbf{x})}{\partial \mathbf{x}} \Big|_{\mathbf{x}=\hat{\mathbf{x}}^{(m)}(t)} \mathcal{L}_1(\Delta_\beta^{(m)}, \gamma_1) \right] \quad (39a)$$

$$\hat{\gamma}_1^{(m)}(t + 1) = \hat{\gamma}_1^{(m)}(t) - \frac{\alpha(t)}{m} \quad (39b)$$

where $\alpha(t)$ is a time-variant iteration step, and $\mathcal{P}_X[\hat{x}]$ denotes the projection of a vector \hat{x} on a closed convex set X , i.e.

$$\mathcal{P}_X[\hat{x}] = \arg \min_{x \in X} \|\hat{x} - x\| \quad (40)$$

When the iteration shown in Eq. (39) is computed, the decision variables $\hat{\mathbf{x}}^{(m)}$ held by the corresponding nodes are updated until the convergence occurs.

Lemma 1. The term $\left\| \frac{\partial \Delta_\beta^{(m)}(\mathbf{x})}{\partial \mathbf{x}} \right\|$ is bounded and $\Delta_\beta^{(m)}(\mathbf{x})$ is a convex function.

Proof. Presenting the decision vector $\mathbf{x} = [x_1, x_2, \dots, x_{(n-6)}]^\top$, the specific form of $\Delta_\beta^{(m)}(\mathbf{x})$ shown in Eq. (32) can be written as

$$\Delta_\beta^{(m)}(\mathbf{x}) = \left\{ \mathbf{H}^\dagger \delta_\beta \right\}_m + \mathbf{V}_\theta(m, 1)x_1 + \dots + \mathbf{V}_\theta(m, n-6)x_{(n-6)} \quad (41)$$

Hence,

$$\frac{\partial \Delta_\beta^{(m)}(\mathbf{x})}{\partial \mathbf{x}} = \begin{bmatrix} \mathbf{V}_\theta(m, 1) \\ \mathbf{V}_\theta(m, 2) \\ \vdots \\ \mathbf{V}_\theta(m, n-6) \end{bmatrix} \quad (42)$$

It is obvious that

$$\left\| \frac{\partial \Delta_\beta^{(m)}(\mathbf{x})}{\partial \mathbf{x}} \right\| \leq C$$

where C is a scalar constant.

According to Eq. (42), the entries of the Hessian matrix of $\Delta_\beta^{(m)}(\mathbf{x})$ are all 0, which implies that $\Delta_\beta^{(m)}(\mathbf{x})$ is a convex function. It also guarantees that the optimization problem in (33) is a convex problem, which can be regarded as a special case of the Lemma 3 in [50]. This concluded the proof. \square

Theorem 1. Based on Lemma 1, if the step size $\alpha(t)$ in Eq. (39b) satisfies

$$\sum_{t=0}^{\infty} \alpha(t) = \infty, \sum_{t=0}^{\infty} \alpha^2(t) < \infty \quad (43)$$

the estimates $\hat{\mathbf{x}}^{(m)}(t)$ and $\hat{\gamma}_1^{(m)}$ for all cellular thruster modules updated by Eq. (39a) and Eq. (39b) can converge to a common optimal solution \mathbf{x}^* and γ_1^* , which are the solution of Eq. (33).

For a proof, see [50].

3.3. Norm-based distributed pseudo-inverse optimal thrust allocation

In this section, a novel cost function for spacecraft control allocation using cellular thruster modules is addressed. The iteration algorithm used in Section 3.2 is also adopted to solve the optimal control allocation problem with the new cost function in a distributed manner.

Formulate a novel matrix $\tilde{\mathbf{A}} \in \mathbb{R}^{n \times 12}$ based on the \mathbf{H}^\dagger and \mathbf{V}_θ as

$$\tilde{\mathbf{A}}(\tilde{\mathbf{x}}) = \left[\mathbf{H}^\dagger, -\mathbf{H}^\dagger \right] + \mathbf{V}_\theta \tilde{\mathbf{x}} \quad (44)$$

where $\tilde{\mathbf{x}} \in \mathbb{R}^{(n-6) \times 12}$ is herein the decision variable. Let $\tilde{\delta}_m$ be a $1 \times n$ vector whose m -th element is 1 and all other elements are all 0. A novel cost function is proposed by choosing m -th row from $\tilde{\mathbf{A}}(\tilde{\mathbf{x}})$ as

$$\tilde{\Delta}^{(m)}(\tilde{\mathbf{x}}) = \|\tilde{\delta}_m (\left[\mathbf{H}^\dagger, -\mathbf{H}^\dagger \right] + \mathbf{V}_\theta \tilde{\mathbf{x}})\|_2^2, \quad (m = 1, 2, \dots, n) \quad (45)$$

where $\|\cdot\|_2$ indicates the 2-norm of vector. The optimal distribution matrix \mathbf{D} is determined as

$$\begin{aligned} \mathbf{D} &= \min_{\tilde{\mathbf{x}}} \max_m \left[\tilde{\Delta}^{(1)}, \dots, \tilde{\Delta}^{(m)}, \dots, \tilde{\Delta}^{(n)} \right]^\top \\ \text{s.t. } \mathbf{V}_\theta \tilde{\mathbf{x}} &\geq \left[\mathbf{H}^\dagger, -\mathbf{H}^\dagger \right] \end{aligned} \quad (46)$$

To obtain \mathbf{D} in Eq. (46) via n cellular thruster modules in the distributed manner, the undirected graph $\mathcal{G} = \{\mathcal{V}, \mathcal{E}\}$ used in Section 3.2 still describes the topology. Also, the node $m \in \mathcal{V}$ is referred to the cellular thruster module $m(m = 1, \dots, n)$. To solve the optimal problem

(46), let $\hat{\mathbf{x}}_m \in \mathbb{R}^{(n-6) \times 12}$ be the estimation of \mathbf{x}^* of node m . The optimal estimation \mathbf{x}^* will be reached through a distributed algorithm that is studied hereinafter. The optimal problem in Eq. (46) is rewritten as

$$\tilde{\mathbf{x}}^* = \arg \min_{\tilde{\mathbf{x}} \in \Upsilon_2} \max_{m \in \mathcal{V}} \tilde{\Delta}^{(m)}, \quad \mathbf{D} = \tilde{\Delta}(\tilde{\mathbf{x}}^*) \quad (47)$$

where the constraint set of $\tilde{\mathbf{x}}$ is $\Upsilon_2 = \{\tilde{\mathbf{x}} | \mathbf{V}_6 \tilde{\mathbf{x}} \geq [\mathbf{H}^\dagger, -\mathbf{H}^\dagger]\}$. The cost function $\tilde{\Delta}^{(m)}$ is held by the cellular thruster module m . Using another decision variable $\gamma_2 \in \mathbb{R}$ in the similar way as Eq. (34), the distributed optimization in (47) is equivalent to

$$\begin{aligned} \min \quad & \gamma_2 \\ \text{s.t.} \quad & \tilde{\Delta}^{(m)}(\tilde{\mathbf{x}}) \leq \gamma_2, \forall \tilde{\mathbf{x}} \in \Upsilon_2, m \in \mathcal{V} \end{aligned} \quad (48)$$

in term of optimal solution $\tilde{\mathbf{x}}^*$. Reform the constraint in Eq. (48) as [50]:

$$\min_{\tilde{\mathbf{x}} \in \Upsilon_2, \gamma_2 \in \mathbb{R}} \gamma_2 + \sum_{m=1}^n \kappa_m \tilde{\Theta}^{(m)}(\tilde{\mathbf{x}}, \gamma_2) \quad (49)$$

where $\tilde{\Theta}^{(m)}(\tilde{\mathbf{x}}, \gamma_2) = \max \left\{ \tilde{\Delta}^{(m)}(\tilde{\mathbf{x}}) - \gamma_2, 0 \right\}$ can penalize the violation of the constraint $\tilde{\Delta}^{(m)}(\tilde{\mathbf{x}}) \leq \gamma_2$ set in Eq. (48). And $\kappa_m > 1$ is the corresponding multiplier based on [50]. Denote the decision variables of cellular thruster module $m (m \in \mathcal{V})$ in a topology \mathcal{G} at the time t as $\tilde{\mathbf{x}}^{(m)}(t) \in \mathbb{R}^{(n-6) \times 12}$ and $\gamma_2^{(m)}(t) \in \mathbb{R}^1$. As the similar exchange way, all decision variables are communicated and transmitted with their neighbors \mathcal{N}_m as [50]

$$\begin{aligned} \hat{\mathbf{x}}^{(m)}(t) &= \sum_{j \in \mathcal{N}_m} a_{mj} \tilde{\mathbf{x}}^{(m)}(t) \\ \hat{\gamma}_2^{(m)}(t) &= \sum_{j \in \mathcal{N}_m} a_{mj} \gamma_2^{(m)}(t) \end{aligned} \quad (50)$$

where a_{mj} is also the entry of the doubly stochastic matrix \mathbf{A} as shown in Eq. (37).

These decision variables are iterated at the time $t + 1$ as [50]:

$$\hat{\mathbf{x}}^{(m)}(t+1) = \mathcal{P}_{\Upsilon_2} \left[\hat{\mathbf{x}}^{(m)}(t) - \alpha(t) \kappa_m \frac{\partial \tilde{\Delta}^{(m)}(\tilde{\mathbf{x}})}{\partial \tilde{\mathbf{x}}} \Big|_{\tilde{\mathbf{x}}=\hat{\mathbf{x}}^{(m)}(t)} \mathcal{L}_2(\tilde{\Delta}^{(m)}, \gamma_2) \right] \quad (51a)$$

$$\hat{\gamma}_2^{(m)}(t+1) = \hat{\gamma}_2^{(m)}(t) - \frac{\alpha(t)}{m} \quad (51b)$$

with the logical function $\mathcal{L}_2(\tilde{\Delta}^{(m)}, \gamma_2)$ defined as

$$\mathcal{L}_2(\tilde{\Delta}^{(m)}, \gamma_2) = \begin{cases} 1 & \tilde{\Delta}^{(m)} \geq \gamma_2 \\ 0 & \tilde{\Delta}^{(m)} < \gamma_2 \end{cases} \quad (52)$$

Lemma 2. The term $\left\| \frac{\partial \tilde{\Delta}_\beta^{(m)}(\tilde{\mathbf{x}})}{\partial \tilde{\mathbf{x}}} \right\|$ is bounded and $\tilde{\Delta}_\beta^{(m)}(\tilde{\mathbf{x}})$ is a convex function.

Proof. Take the decision vector

$$\tilde{\mathbf{x}} = \begin{bmatrix} \tilde{x}(1, 1) & \tilde{x}(1, 2) & \dots & \tilde{x}(1, 12) \\ \vdots & \vdots & \vdots & \vdots \\ \tilde{x}(n-6, 1) & \tilde{x}(n-6, 2) & \dots & \tilde{x}(n-6, 12) \end{bmatrix}$$

Referred to the proof of Lemma 1, substitute $\tilde{\mathbf{x}}$ into Eq. (45) and take partial derivative of $\tilde{\Delta}_\beta^{(m)}(\tilde{\mathbf{x}})$ with respect to $\tilde{\mathbf{x}}$ to obtain $\frac{\partial \tilde{\Delta}_\beta^{(m)}(\tilde{\mathbf{x}})}{\partial \tilde{\mathbf{x}}}$. Since $\tilde{\mathbf{x}}$ is bounded, it is easy to have:

$$\left\| \frac{\partial \tilde{\Delta}_\beta^{(m)}(\tilde{\mathbf{x}})}{\partial \tilde{\mathbf{x}}} \right\| \leq \tilde{C}$$

where \tilde{C} is a scalar constant. Also, the entries of Hessian matrix of $\tilde{\Delta}(\tilde{\mathbf{x}})$ are greater than 0, which implies that $\tilde{\Delta}^{(m)}(\tilde{\mathbf{x}})$ is a convex function. It also guarantees that the optimization problem in (47) is a convex problem [50]. This concluded the proof. \square

Note that Theorem 1 is also applied on the iteration process shown in Eq. (51). It indicates that the step size α satisfies Eq. (43). Then, the optimal solution \mathbf{x}^* can be yielded by calculating the iteration process in Eqs. (50)(51).

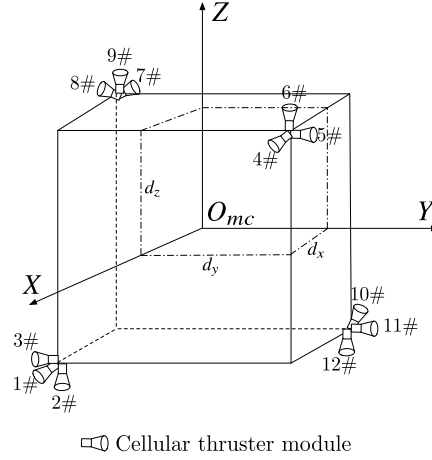


Fig. 3. Configuration of cellular thruster modules.

3.4. Synthesis of distributed optimal thrust allocation

Recall the 6-dof dynamics of the rigid-body spacecraft in Eq. (16). The general control input $\Gamma_c = [\mathbf{t}_c^T, \mathbf{f}_c^T]^T$ is the high-level control signal which would be subsequently distributed to different cellular thruster modules under the proposed thrust allocation schemes. Since the main focus of this paper is to develop the distributed thrust allocation schemes, the conventional proportional-derivative controller [20] is used in this paper to generate Γ_c :

$$\Gamma_c = -\mathbf{K}_p \boldsymbol{\eta} - \mathbf{K}_d \dot{\boldsymbol{\xi}} \quad (53)$$

where $\mathbf{K}_p \in \mathbb{R}^{6 \times 6} > 0$ and $\mathbf{K}_d \in \mathbb{R}^{6 \times 6} > 0$ are the proportional and derivative parameters respectively. By dividing the scalar l as Eq. (21), the high-level signal Γ_c is converted into $\tilde{\Gamma}_c$. According to Eq. (22), $\tilde{\Gamma}_c$ can be extended to the pure-positive vector $\tilde{\Gamma}_c^\oplus$. Then, solve the optimal problems shown in Eq. (30) or Eq. (46) by the proposed distributed algorithms which are displayed in Eq. (39) or Eq. (51) to have the optimal distributed matrix \mathbf{D} . The thrust that each cellular thruster module should produce can be calculated through Eq. (24). When the thrusts $\boldsymbol{\tau}$ are multiplied with the cellular thruster modules' configuration matrix \mathbf{H} , the actual torques and forces $\Gamma_{c,actual}$ can be obtained from $\Gamma_{c,actual} = \mathbf{H} \boldsymbol{\tau}$, as shown in Eq. (19), and then serve as the inputs of 6-dof spacecraft dynamics in Eq. (16).

4. Numerical simulations

In this section, the proposed two distributed thrust allocation schemes for 6-dof spacecraft maneuvering are verified through numerical simulations. The mass of the rigid spacecraft is $m = 100$ kg. Spacecraft's moment of inertia is $\mathbf{I} = \text{diag}\{20, 20, 20\}$ kg · m². The initial translation error $\boldsymbol{\rho}_0 = [15, -10, -20]^T$ m. The initial value for $\boldsymbol{\xi}$ is set as $\boldsymbol{\xi}_0 = \mathbf{0}$. The initial attitude of the rigid-body spacecraft is given in the form of Euler angles which is set as $[45^\circ, 45^\circ, -45^\circ]$ with rotation sequence "zxz". The external disturbances in Eq. (16) are set as

$$\mathbf{t}_d = [0.025 \sin(0.2t), 0.028 \sin(0.2t), 0.023 \sin(0.25t)]^T \text{ N} \cdot \text{m}$$

$$\mathbf{f}_d = [0.005 \cos(0.2t), 0.008 \sin(0.25t), -0.003 \sin(0.3t)]^T \text{ N}$$

The control parameters in the proportional-derivative controller in Eq. (53) are

$$\mathbf{K}_p = \text{diag}\{0.1, 0.1, 0.1, 0.15, 0.15, 0.15\}, \quad \mathbf{K}_d = \text{diag}\{2.9, 2.9, 2.9, 6, 6, 6\}$$

The spacecraft is operating in a circular orbit whose orbital inclination is 45° , true anomaly is 70° , longitude of the ascending node is 120° , argument of periapsis is 60° , and semi-major axis is 400 km.

In simulation, there are 12 cellular thruster modules are installed at the different places of the rigid-body spacecraft, which is depicted as Fig. 3. This configuration is adopted from the generic thruster placement, such as [13]. The cellular thruster modules' configuration matrices $\mathbf{H} = [\mathbf{H}_\tau^T, \mathbf{H}_f^T]^T$ are given as follows.

$$\mathbf{H}_\tau = \begin{bmatrix} 0 & d_z & -d_y & 0 & d_z & -d_y & 0 & -d_z & d_y & 0 & -d_z & d_y \\ d_z & 0 & -d_x & -d_z & 0 & d_x & d_z & 0 & -d_x & -d_z & 0 & d_x \\ -d_y & d_x & 0 & d_y & -d_x & 0 & d_y & -d_x & 0 & -d_y & d_x & 0 \end{bmatrix}$$

$$\mathbf{H}_f = \begin{bmatrix} -1 & 0 & 0 & -1 & 0 & 0 & 1 & 0 & 0 & 1 & 0 & 0 \\ 0 & 1 & 0 & 0 & -1 & 0 & 0 & 1 & 0 & 0 & -1 & 0 \\ 0 & 0 & 1 & 0 & 0 & -1 & 0 & 0 & -1 & 0 & 0 & 1 \end{bmatrix}$$

where $d_x = d_y = d_z = 0.5$ m. The scalar factor in Eq. (21) is selected as $l = 1$ m.

All 12 cellular thruster modules are viewed as the nodes in the graph \mathcal{G} . These nodes are connected through a chain topology shown in Fig. 4, in which the squares represent the cellular thruster modules and the line stands for the communication link between each

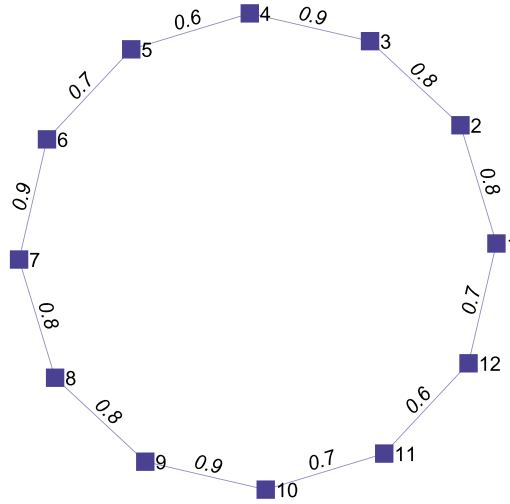


Fig. 4. Topology of cellular thruster modules: chain shape.

cellular thruster module. The proposed iteration algorithm shown in Eqs. (36)(39) or Eqs. (50)(51) are implemented to solve the optimal distributed matrix \mathbf{D} using Eq. (30) or Eq. (46) respectively. The parameter κ_m is set as 2.5 either in Eq. (39a) or Eq. (51a). The iteration step α in both equations is set as $\alpha(t) = 1/t^{0.1}$. The weight matrix in either Eq. (36) or Eq. (50) is given by

$$\mathbf{A} = (\mathbf{1}_{n \times n} + \mathbf{L}_w)^{-1} \quad (54)$$

where $\mathbf{1}_{n \times n}$ is an $n \times n$ identity matrix (n is the total number of cellular thruster modules), \mathbf{L}_w is the weighted Laplacian matrix and is calculated as $\mathbf{L}_w = \mathbf{B}\mathbf{W}\mathbf{B}^T$ [51]. Here, \mathbf{B} is the incidence matrix of graph \mathcal{G} . $\mathbf{W} = \text{diag}\{w_{ij}\}$ is the edge weight matrix of \mathcal{G} . The edge weight w_{ij} can be obtained from the number close to each edge in Fig. 4.

4.1. Simulation for 6-dof spacecraft maneuver under the distributed thrust allocation schemes

For the sake of clarity, the distributed pseudo-inverse thrust allocation scheme which is studied in Section 3.2, is labeled as “scheme 1”. The norm-based pseudo-inverse thrust allocation scheme in Section 3.3 is labeled as “scheme 2” in the following simulation results. Define the error between the desired control input $\mathbf{\Gamma}_c$ before thrust allocation and actual control input $\mathbf{\Gamma}_{c,actual}$ after thrust allocation as

$$\mathbf{e} = \mathbf{\Gamma}_c - \mathbf{\Gamma}_{c,actual} = [e_1, e_2, e_3, e_4, e_5, e_6]^T \quad (55)$$

The time responses of \mathbf{e} using “scheme 1” and “scheme 2” are shown in Fig. 5 and Fig. 6 respectively. Both Fig. 5 and Fig. 6 indicate that the errors \mathbf{e} are sufficient small. It can guarantee that the stability of 6-dof spacecraft dynamics is not adversely affected. These small errors show that both distributed thrust allocation schemes are effective. The gaps between the high-level control signals and the low-level control ones are quite close. This is a common feature for both schemes. The sufficient small \mathbf{e} induces stable 6-dof control performance for the rigid-body spacecraft maneuvering. Note that the errors defined in Eq. (55) is worth to be discussed since the matrix \mathbf{D} does not simply equal to the pseudoinverse of \mathbf{H} in the processes of $\boldsymbol{\tau} = \mathbf{D}\tilde{\mathbf{\Gamma}}_c^\oplus$ and $\mathbf{\Gamma}_{c,actual} = \mathbf{H}\boldsymbol{\tau}$.

Since \mathbf{e} from “scheme 1” and “scheme 2” are all quite small, only one group of time responses of $\boldsymbol{\varphi}$, $\boldsymbol{\phi}$, $\Delta\mathbf{v}$, $\Delta\boldsymbol{\omega}$ are shown as Figs. 7-10 when either “scheme 1” or “scheme 2” is served as the thrust allocation scheme.

However, the norm-based scheme (“scheme 2”) has smaller cumulative errors compared with “scheme 1”. This fact can be confirmed by calculating the 1-norm-index of error \mathbf{e} defined as

$$\|e_i(t)\|_{l_1} = \int_0^t \|e_i(\hat{t})\|_1 d\hat{t} \quad (i = 1, 2, \dots, 6) \quad (56)$$

Fig. 11 shows that $\|e_i(t)\|_{l_1}$ under “scheme 1” is much greater than them under “scheme 2”. In Fig. 12, all the thrusts calculated by “scheme 1” for 12 cellular thruster modules are larger than the thrusts calculated by “scheme 2”. It indicates that the optimal results under “scheme 2” are better than the results under “scheme 1”. Additionally, energy consumption is very crucial to evaluate the performances of different thrust allocation schemes since it stands for how much fuels that would be consumed. The thruster cost $\mathcal{E}(t)$ related to the energy consumption is defined as

$$\mathcal{E}(t) = \int_0^t \|\boldsymbol{\tau}(\tilde{t})\|_2 d\tilde{t} \quad (57)$$

The results of the thrust cost norm $\mathcal{E}(t)$ are shown in Fig. 13. These all demonstrate that the norm-based distributed thrust allocation scheme (“scheme 2”) is better than the general pseudo-inverse thrust allocation scheme (“scheme 1”).

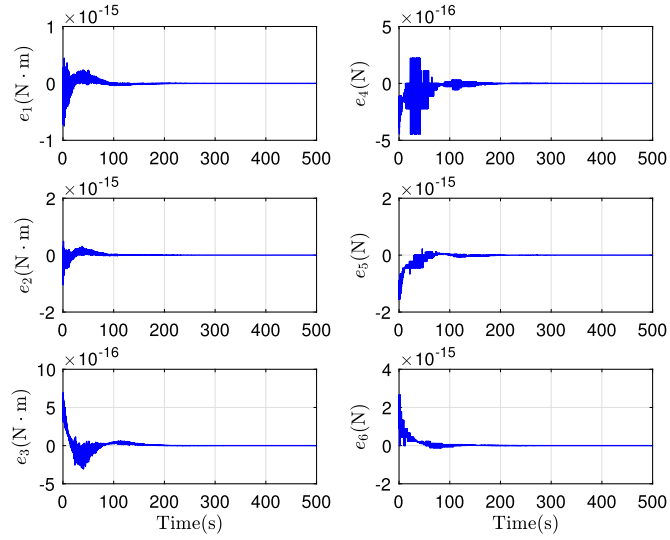


Fig. 5. Time response of \mathbf{e} using scheme 1.

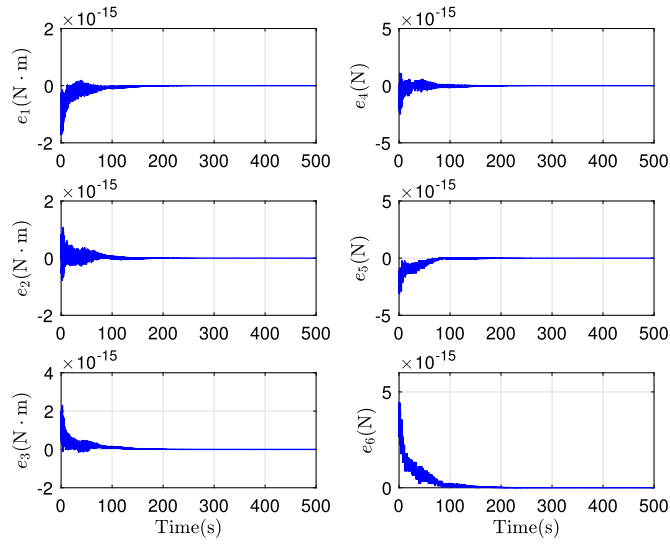


Fig. 6. Time response of \mathbf{e} using scheme 2.

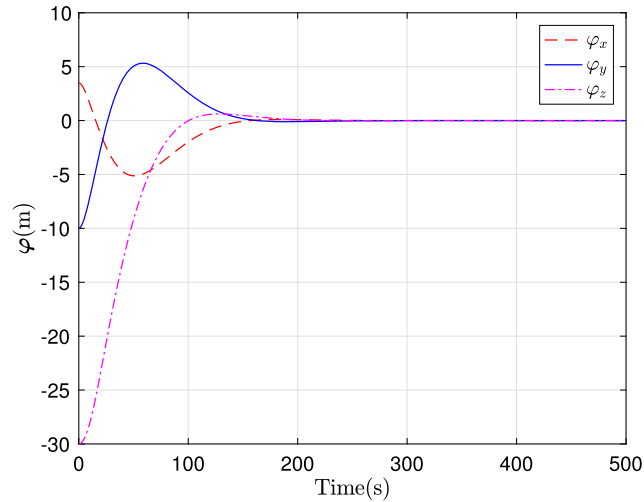


Fig. 7. Time response of $\boldsymbol{\varphi}$.

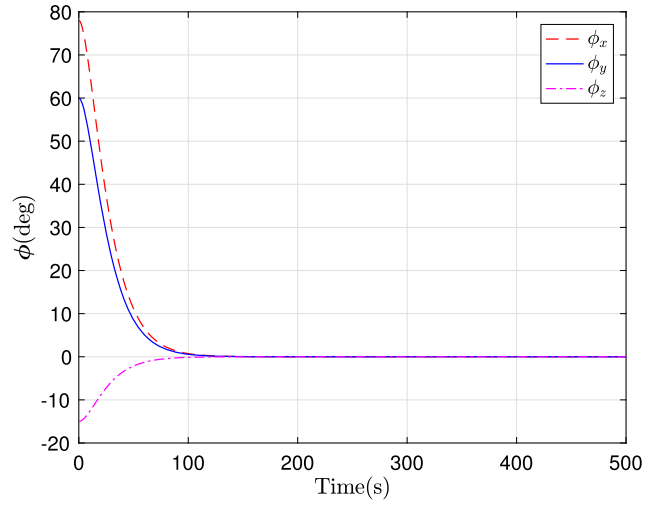


Fig. 8. Time response of ϕ .

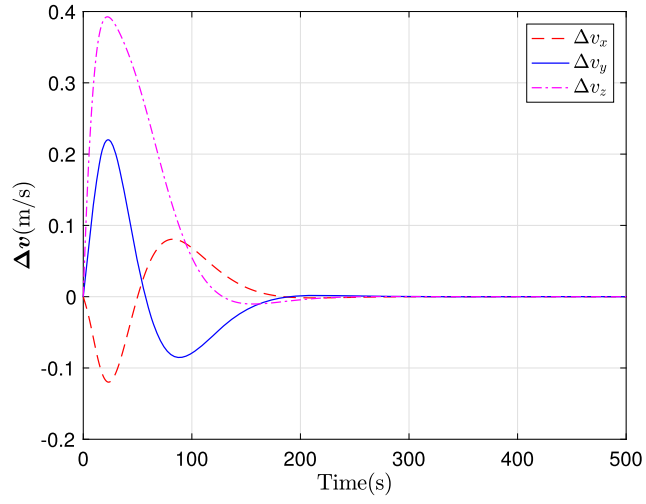


Fig. 9. Time response of Δv .

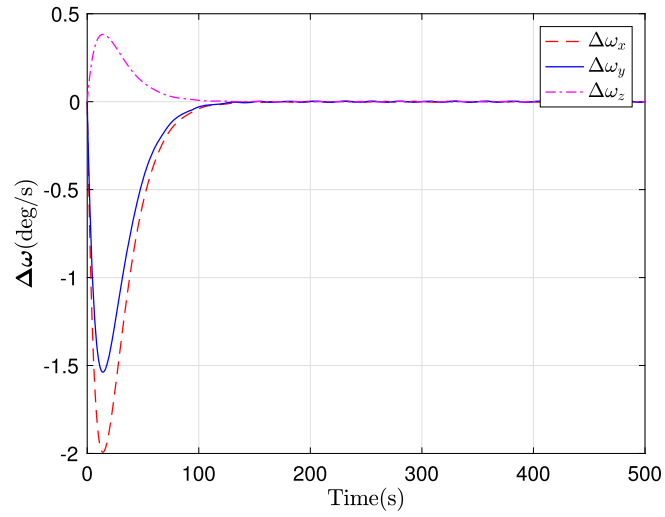


Fig. 10. Time response of $\Delta \omega$.

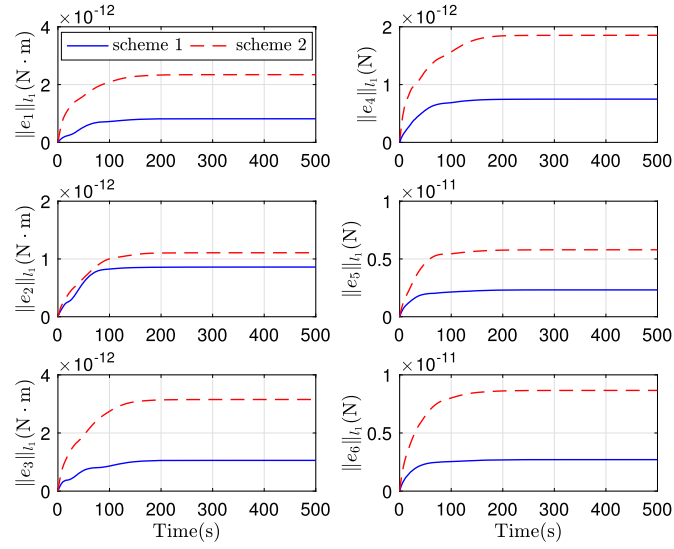


Fig. 11. Time response of $\|e\|_{l_1}$.

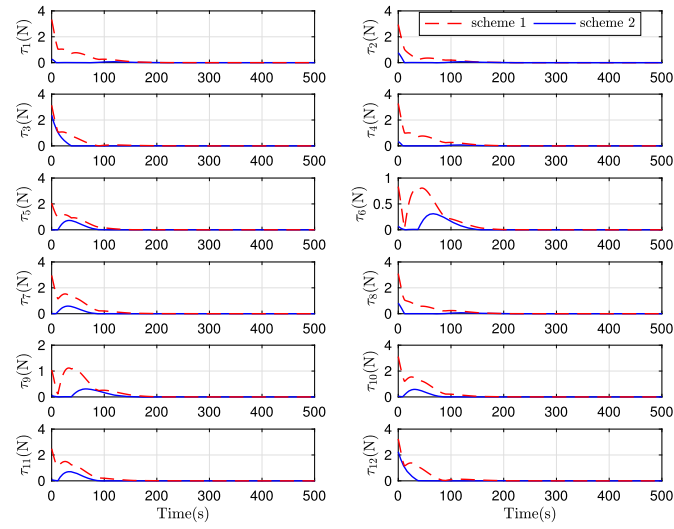


Fig. 12. Thrust from control allocation.

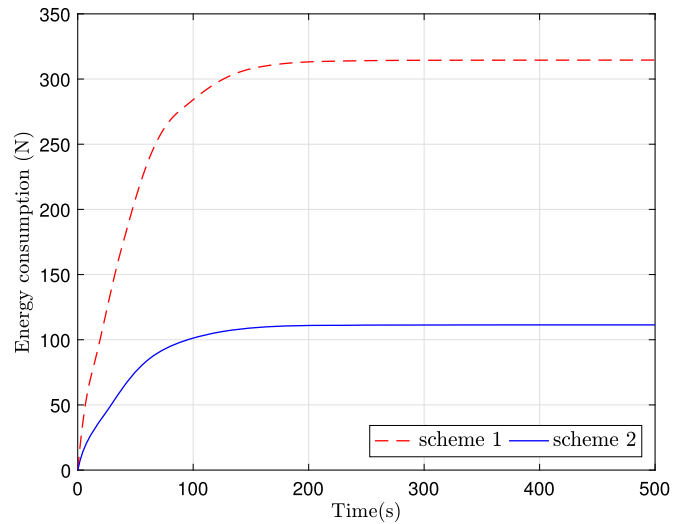


Fig. 13. Energy consumption.

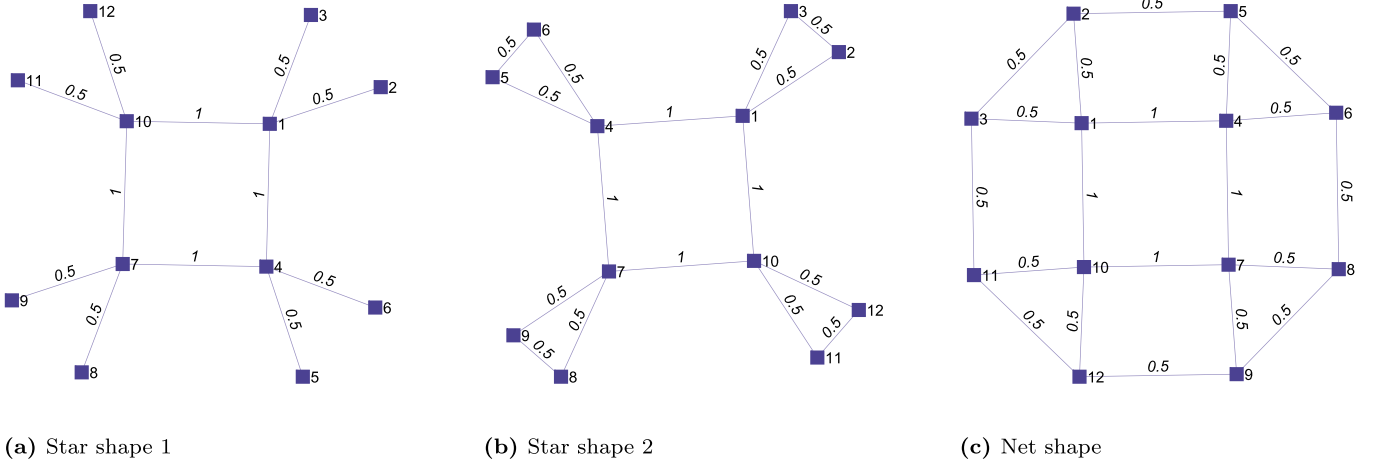


Fig. 14. Three topologies.

Table 1

Performance comparison between different topology structures.

Parameter	Chain shape (Fig. 4)	Star shape 1 (Fig. 14a)	Star shape 2 (Fig. 14b)	Net shape (Fig. 14c)	All-connected shape
Edge number	12	12	16	20	66
Convergence step	63	71	75	69	62
$\ \mathbf{e}(t_f)\ _2$ (N)	2.3155×10^{-9}	2.0497×10^{-9}	2.6417×10^{-9}	2.4442×10^{-9}	2.3191×10^{-9}
$\mathcal{E}(t_f)$	135.4933	148.2194	148.7598	148.6398	148.3915
τ_{\max} (N)	2.3713	2.4546	2.5010	2.4549	2.4558

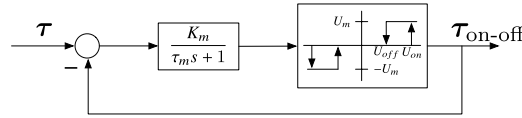


Fig. 15. Pulse-width pulse-frequency (PWPF) modulator.

4.2. Topology sensitivity analysis

All above simulation results are carried out on the basis of the topology shown in Fig. 4. There are still some alternative connections among different cellular thruster modules. They are depicted in Fig. 14. Different topologies have different edge weights w_{ij} which are used to form different matrix \mathbf{A} defined in Eq. (54).

With the different matrices \mathbf{A} , the iteration proposed in Eqs. (50)(51) can generate different matrices for \mathbf{D} which are used for thrust allocation. Some performance comparison results are summarized in Table 1 for norm-based pseudo-inverse optimal thrust allocation with different topologies. The “all-connected shape” in Table 1 indicates that all cellular thruster modules (nodes) are connected with each other and each edge's weight $w_{ij} = 1$.

From Table 1, the topology with chain shape in Fig. 4 has the smallest value in terms of the maximum thrust τ_{\max} . It also has the smallest total thrust cost index $\mathcal{E}(t_f)$ (t_f is the terminal time of simulation) compared with other shapes. The small convergence step is almost the same as that of “all-connected shape”. The “star shape 1” in Fig. 14a has the same communication link number as that of the chain shape. The convergence step of “star shape 1” is large but the 2-norm-index $\|\mathbf{e}(t_f)\|_2$ is the smallest one among all studied topology structures. For total thrust cost, all topology shapes except the chain shape have large values that are almost equal. The “star shape 2” (Fig. 14b) and the net shape (Fig. 14c) have similar poor performance for all parameters except the number of edge. For the “all-connected shape”, it has the smallest convergence steps but has the most edge numbers. Overall, it can be determined that the chain shape and the “star shape 1” are most valuable topologies to be used.

4.3. On-off signal generation

The thrusts yielded from either “scheme 1” or “scheme 2” are all continuous signals. In practical applications, however, the common thrusters need on-off commands to produce thrusts. The pulse-width pulse-frequency (PWPF) modulator is employed in this work to make the proposed thrust allocation scheme more applicable. Since the control allocation performance of “scheme 2” is better than “scheme 1”, the continuous thrusts signals from “scheme 2” are selected to be converted into on-off signals through PWPF modulator. The PWPF modulator [52] is made up of a first-order filter, a Schmitt trigger and a feedback loop, which is diagrammed as Fig. 15 [52].

The corresponding parameters of the PWPF modulator are set as: $K_m = 2$, $\tau_m = 0.6$, $U_{on} = 0.008$, $U_{off} = 0.6 \times U_{on}$, $U_m = 1$. Under this PWPF modulator, the continuous thrust signals yielded from “scheme 2” are converted into the discrete control commands as shown in Fig. 16.

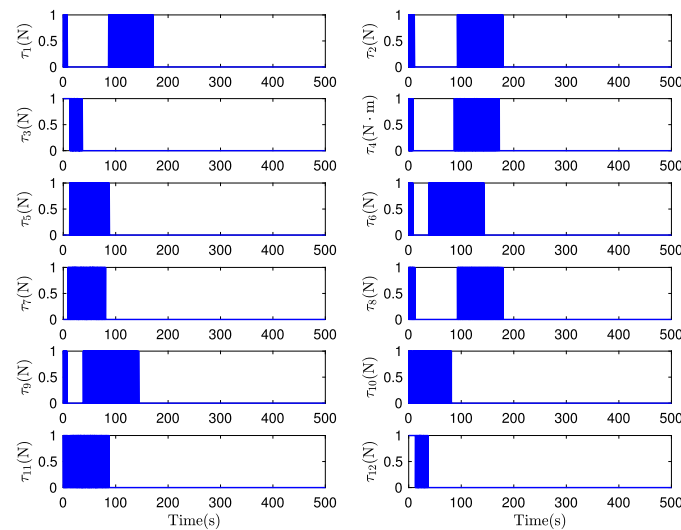


Fig. 16. On-off thrusts using pulse-width pulse-frequency (PWPF) modulator.

5. Conclusions

This paper proposes two distributed thrust allocation schemes for 6-dof spacecraft maneuvers using multiple cellular thruster modules. The contribution of this paper is two-fold. The first one is that the pseudo-inverse optimal thrust allocation is extended and can be executed in a distributed manner. The second one is developing a norm-based distributed pseudo-inverse optimal thrust allocation scheme. The numerical simulations not only validate the effectiveness of the two distributed thrust allocation schemes, but also demonstrate that the norm-based scheme has lower thrust cost level as well as smaller magnitudes of thrust compared with the first scheme. Several alternatives topology structures are analyzed by comparing some key indices which can characterize the performances of two thrust allocation schemes.

Declaration of competing interest

No competing interest.

Acknowledgements

This work is supported by the Canada Research Chairs program, Grant number 950-230883.

References

- [1] A. Flores-Abad, O. Ma, K. Pham, S. Ulrich, A review of space robotics technologies for on-orbit servicing, *Prog. Aerosp. Sci.* 68 (2014) 1–26, <https://doi.org/10.1016/j.paerosci.2014.03.002>.
- [2] N. Inaba, M. Oda, M. Asano, Rescuing a stranded satellite in space—experimental robotic capture of non-cooperative satellites, *Trans. Jpn. Soc. Aeronaut. Space Sci.* 48 (162) (2006) 213–220, <https://doi.org/10.2322/tjsass.48.213>.
- [3] M. Jankovic, J. Paul, F. Kirchner, Gnc architecture for autonomous robotic capture of a non-cooperative target: preliminary concept design, *Adv. Space Res.* 57 (8) (2016) 1715–1736, <https://doi.org/10.1016/j.asr.2015.05.018>.
- [4] D. Barnhart, B. Sullivan, Economics of repurposing in situ retired spacecraft components, in: *AIAA SPACE 2012 Conference & Exposition*, 2012–5304, <https://doi.org/10.2514/6.2012-5304>.
- [5] J. Weise, K. Brieß, A. Adomeit, H.-G. Reimerdes, M. Göller, R. Dillmann, An intelligent building blocks concept for on-orbit-satellite servicing, in: *Proceedings of the International Symposium on Artificial Intelligence, Robotics and Automation in Space (ISAIRAS)*, 2012.
- [6] F. Zhang, G. Duan, Robust adaptive integrated translation and rotation control of a rigid spacecraft with control saturation and actuator misalignment, *Acta Astronaut.* 86 (2013) 167–187, <https://doi.org/10.1016/j.actaastro.2013.01.010>.
- [7] Y. Huang, Y. Jia, Adaptive finite-time 6-dof tracking control for spacecraft fly around with input saturation and state constraints, *IEEE Trans. Aerosp. Electron. Syst.* 55 (6) (2019) 3259–3272, <https://doi.org/10.1109/taes.2019.2906096>.
- [8] M. Wang, Y. Xie, Design of the optimal thruster combinations table for the real time control allocation of spacecraft thrusters, in: *Proceedings of the 48th IEEE Conference on Decision and Control (CDC) Held Jointly with 2009 28th Chinese Control Conference, IEEE, 2009*, pp. 5063–5068.
- [9] D. Zhou, Y. Zhang, S. Li, Receding horizon guidance and control using sequential convex programming for spacecraft 6-dof close proximity, *Aerosp. Sci. Technol.* 87 (2019) 459–477, <https://doi.org/10.1016/j.ast.2019.02.041>.
- [10] Y. Huang, Y. Jia, Integrated robust adaptive tracking control of non-cooperative fly-around mission subject to input saturation and full state constraints, *Aerosp. Sci. Technol.* 79 (2018) 233–245, <https://doi.org/10.1016/j.ast.2018.05.033>.
- [11] J. Zhang, J.D. Biggs, D. Ye, Z. Sun, Finite-time attitude set-point tracking for thrust-vectoring spacecraft rendezvous, *Aerosp. Sci. Technol.* 96 (2020) 105588, <https://doi.org/10.1016/j.ast.2019.105588>.
- [12] Y. Wang, H. Ji, Integrated relative position and attitude control for spacecraft rendezvous with iss and finite-time convergence, *Aerosp. Sci. Technol.* 85 (2019) 234–245, <https://doi.org/10.1016/j.ast.2018.12.005>.
- [13] F. Curti, M. Romano, R. Bevilacqua, Lyapunov-based thrusters' selection for spacecraft control: analysis and experimentation, *J. Guid. Control Dyn.* 33 (4) (2010) 1143–1160, <https://doi.org/10.2514/1.47296>.
- [14] Q. Hu, W. Chen, Y. Zhang, Concurrent proximity control of servicing spacecraft with an uncontrolled target, *IEEE/ASME Trans. Mechatron.* 24 (6) (2019) 2815–2826, <https://doi.org/10.1109/tmech.2019.2944387>.
- [15] B. Shasti, A. Alasty, N. Assadian, Robust distributed control of spacecraft formation flying with adaptive network topology, *Acta Astronaut.* 136 (2017) 281–296, <https://doi.org/10.1016/j.actaastro.2017.03.001>.

- [16] J. Wang, Z. Sun, 6-dof robust adaptive terminal sliding mode control for spacecraft formation flying, *Acta Astronaut.* 73 (2012) 76–87, <https://doi.org/10.1016/j.actaastro.2011.12.005>.
- [17] N. Filipe, P. Tsiotras, Adaptive position and attitude-tracking controller for satellite proximity operations using dual quaternions, *J. Guid. Control Dyn.* 38 (4) (2015) 566–577, <https://doi.org/10.2514/1.g000054>.
- [18] H. Gui, G. Vukovich, Finite-time output-feedback position and attitude tracking of a rigid body, *Automatica* 74 (2016) 270–278, <https://doi.org/10.1016/j.automatica.2016.08.003>.
- [19] K. Gong, Y. Liao, Y. Wang, Adaptive fixed-time terminal sliding mode control on se (3) for coupled spacecraft tracking maneuver, *Int. J. Aerosp. Eng.* 2020 (2020), <https://doi.org/10.1155/2020/3085495>.
- [20] F. Bullo, R.M. Murray, Proportional derivative (pd) control on the Euclidean group, in: *European Control Conference*, vol. 2, 1995, pp. 1091–1097.
- [21] J. Zhang, D. Ye, Z. Sun, C. Liu, Extended state observer based robust adaptive control on se (3) for coupled spacecraft tracking maneuver with actuator saturation and misalignment, *Acta Astronaut.* 143 (2018) 221–233, <https://doi.org/10.1016/j.actaastro.2017.11.034>.
- [22] M. Tavakoli, N. Assadian, Predictive fault-tolerant control of an all-thruster satellite in 6-dof motion via neural network model updating, *Adv. Space Res.* 61 (6) (2018) 1588–1599, <https://doi.org/10.1016/j.asr.2017.12.032>.
- [23] Q. Zhao, G. Duan, Integrated design of trajectory tracking and inertia property identification for post-capture of non-cooperative target, *Aerosp. Sci. Technol.* 95 (2019) 105437, <https://doi.org/10.1016/j.ast.2019.105437>.
- [24] A.H. De Ruiter, C. Damaren, J.R. Forbes, *Spacecraft Dynamics and Control: An Introduction*, John Wiley & Sons, 2012, pp. 506–508.
- [25] T.A. Johansen, T.I. Fossen, Control allocation—a survey, *Automatica* 49 (5) (2013) 1087–1103, <https://doi.org/10.1016/j.automatica.2013.01.035>.
- [26] S.S. Tohidi, A. Khaki Sedigh, D. Buzorgnia, Fault tolerant control design using adaptive control allocation based on the pseudo inverse along the null space, *Int. J. Robust Nonlinear Control* 26 (16) (2016) 3541–3557, <https://doi.org/10.1002/rnc.3518>.
- [27] P. Huang, M. Wang, Z. Meng, F. Zhang, Z. Liu, Attitude takeover control for post-capture of target spacecraft using space robot, *Aerosp. Sci. Technol.* 51 (2016) 171–180, <https://doi.org/10.1016/j.ast.2016.02.006>.
- [28] X. Huang, G.-R. Duan, Dynamic infinity-norm constrained control allocation for attitude tracking control of overactuated combined spacecraft, *IET Control Theory Appl.* 13 (11) (2019) 1692–1703, <https://doi.org/10.1049/iet-cta.2018.5707>.
- [29] X. Huang, J.D. Biggs, G. Duan, Post-capture attitude control with prescribed performance, *Aerosp. Sci. Technol.* 96 (2020) 105572.
- [30] T.A. Johansen, T.I. Fossen, S.P. Berge, Constrained nonlinear control allocation with singularity avoidance using sequential quadratic programming, *IEEE Trans. Control Syst. Technol.* 12 (1) (2004) 211–216, <https://doi.org/10.1109/tcst.2003.821952>.
- [31] Q. Hu, G. Niu, C. Wang, Spacecraft attitude fault-tolerant control based on iterative learning observer and control allocation, *Aerosp. Sci. Technol.* 75 (2018) 245–253, <https://doi.org/10.1016/j.ast.2017.12.031>.
- [32] F. Ankersen, S.F. Wu, A. Aleshin, A. Vankov, V. Volochinov, Optimization of spacecraft thruster management function, *J. Guid. Control Dyn.* 28 (6) (2005) 1283–1290, <https://doi.org/10.2514/1.11531>.
- [33] A. Smith, D. Seo, Spacecraft thruster distribution matrix for precision 6dof control, in: *AIAA SPACE and Astronautics Forum and Exposition*, 2017, p. 5203.
- [34] A. Smith, D. Seo, Optimized thruster distribution matrix for precision 6dof control utilizing dual quaternions dynamics, in: *AIAA 2018 Space Flight Mechanics Meeting*, 2018, p. 0963.
- [35] M. Bodson, Evaluation of optimization methods for control allocation, *J. Guid. Control Dyn.* 25 (4) (2002) 703–711, <https://doi.org/10.2514/6.2001-4223>.
- [36] H. Chang, P. Huang, Y. Zhang, Z. Meng, Z. Liu, Distributed control allocation for spacecraft attitude takeover control via cellular space robot, *J. Guid. Control Dyn.* 41 (11) (2018) 2499–2506, <https://doi.org/10.2514/1.G003626>.
- [37] A.K. Das, M. Mesbahi, Distributed linear parameter estimation over wireless sensor networks, *IEEE Trans. Aerosp. Electron. Syst.* 45 (4) (2009) 1293–1306, <https://doi.org/10.1109/TAES.2009.5310299>.
- [38] A. Nedic, A. Ozdaglar, Distributed subgradient methods for multi-agent optimization, *IEEE Trans. Autom. Control* 54 (1) (2009) 48–61, <https://doi.org/10.1109/tac.2008.2009515>.
- [39] Q. Shen, D. Wang, S. Zhu, E.K. Poh, Inertia-free fault-tolerant spacecraft attitude tracking using control allocation, *Automatica* 62 (2015) 114–121, <https://doi.org/10.1016/j.automatica.2015.09.027>.
- [40] Q. Shen, D. Wang, S. Zhu, E.K. Poh, Robust control allocation for spacecraft attitude tracking under actuator faults, *IEEE Trans. Control Syst. Technol.* 25 (3) (2017) 1068–1075, <https://doi.org/10.1109/tcst.2016.2574763>.
- [41] W. Gai, J. Liu, J. Zhang, Y. Li, A new closed-loop control allocation method with application to direct force control, *Int. J. Control. Autom. Syst.* 16 (3) (2018) 1355–1366, <https://doi.org/10.1007/s12555-017-0294-9>.
- [42] M.A. Silva, M. Shan, A. Cervone, E. Gill, Fuzzy control allocation of microthrusters for space debris removal using cubesats, *Eng. Appl. Artif. Intell.* 81 (2019) 145–156, <https://doi.org/10.1016/j.engappai.2019.02.008>.
- [43] A. Taheri, N. Assadian, Dynamic-programming-based failure-tolerant control for satellite with thrusters in 6-dof motion, *Adv. Space Res.* (2020).
- [44] Q. Hu, X. Tan, Dynamic near-optimal control allocation for spacecraft attitude control using a hybrid configuration of actuators, *IEEE Trans. Aerosp. Electron. Syst.* 56 (2) (2019) 1430–1443, <https://doi.org/10.1109/TAES.2019.2934697>.
- [45] T.D. Barfoot, *State Estimation for Robotics*, Cambridge University Press, 2017.
- [46] S. Brás, M. Izadi, C. Silvestre, A. Sanyal, P. Oliveira, Nonlinear observer for 3d rigid body motion, in: *52nd IEEE Conference on Decision and Control*, IEEE, 2013, pp. 2588–2593.
- [47] D.A. Vallado, *Fundamentals of Astrodynamics and Applications*, vol. 12, Springer Science & Business Media, 2001.
- [48] M. Mesbahi, M. Egerstedt, *Graph Theoretic Methods in Multiagent Networks*, vol. 33, Princeton University Press, 2010.
- [49] D.P. Bertsekas, Necessary and sufficient conditions for a penalty method to be exact, *Math. Program.* 9 (1) (1975) 87–99, <https://doi.org/10.1007/bf01681332>.
- [50] K. Srivastava, A. Nedić, D. Stipanović, Distributed min-max optimization in networks, in: *2011 17th International Conference on Digital Signal Processing (DSP)*, IEEE, 2011, pp. 1–8.
- [51] R. Merris, Doubly stochastic graph matrices, *II, Linear Multilinear Algebra* 45 (2–3) (1998) 275–285, <https://doi.org/10.1080/03081089808818591>.
- [52] F.L. Markley, J.L. Crassidis, *Fundamentals of Spacecraft Attitude Determination and Control*, Springer, New York, 2014, pp. 303–306.